ACS APPLIED MATERIALS & INTERFACES

www.acsami.org

Research Article

Chargeable Hydrogels with Dual Modulatory Effects of Bacterial Killing and Immune Remodeling toward Wound Healing

Yiheng Tang,[⊥] Guopeng Xu,[⊥] Jing Liu,[⊥] Jiezhou Wu, Jingyang Fang, Shengji Gu, Wenyan Zhang, Wenkun Zhang, Junfeng Hu, Paul K. Chu, Jianzhong Du, and Guomin Wang*

Cite This: *ACS Appl. Mater. Interfaces* 2025, 17, 53232−53243

Read Online

ACCESS | Metrics & More | Article Recommendations | Supporting Information

ABSTRACT: Wound infections challenge clinical medicine, and developing novel therapies is critically important in overcoming antimicrobial resistance and an off-balanced immune microenvironment. Electrical stimulation as a biocompatible, easy-to-operate, and controllable technique has great potential in eradicating pathogens and modulating the immune system. However, safe and soft platforms that integrate both bactericidal and immunological modulatory effects of electrical stimulation are rarely reported. In this study, we propose a new strategy targeting infectious wound healing that utilizes chargeable hydrogels as the carrier of electrical stimulation to deploy timely bacterial disinfection and subsequently reprogram the macrophage phenotype. The chargeable platform (AT-PP@MnO_2) is constructed by doping manganese dioxide (MnO_2) microparticles into acid-treated PEDOT:PSS hydrogels (AT-PP), in which MnO_2 acts as the collector for charge storage and release. Upon a safe charging process at 0.8 V, AT-PP@MnO_2 achieves 99% bacterial inactivation within 15 min. The bactericidal mechanism is attributed to charging-evoked electron deprivation from bacteria, inducing an intracellular reactive oxygen species (ROS) burst to damage bacterial structure. Furthermore, the *in vivo* mouse model of wound infection demonstrates that AT-PP@MnO_2 can timely eradicate invasive bacteria to prevent infection from aggravation and then reprogram macrophages from proinflammatory to anti-inflammatory for immune remodeling, thus achieving nearly 100% wound healing within 14 days. This study introduces an emerging physical paradigm to the design of multifunctional wound dressing, offering broad potential in combating bacterial infections and immune modulation.

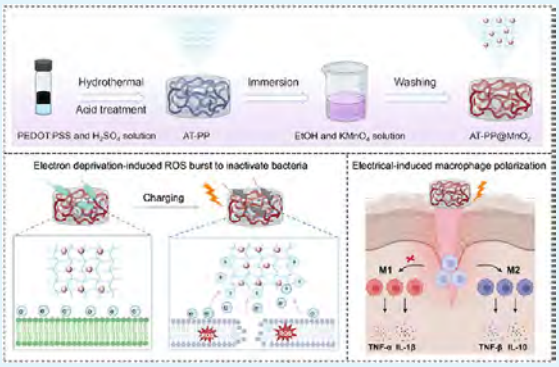

KEYWORDS: *electrical stimulation, wound infection, conductive hydrogel, immune modulation, antibacterial process based on electron transfer*

1. INTRODUCTION

Infected wounds, if left untreated, can progress into life-threatening systemic complications, such as sepsis, irreversible tissue damage, and long-term disability,[1−3] underscoring the critical need for early intervention. The wound healing process involves stages of hemostasis, inflammation, proliferation, and remodeling, among which the inflammation stage is essential due to its role in infection defense, signal repair, and balance control between tissue repair and excessive scar formation.[1,4,5] Bacterial infection emerging in the inflammation process could ruin the wound healing process, because it can cause prolonged inflammation and damage to the surrounding tissues. Immune cells are crucial in fighting infections, but without targeted modulation, they may not be able to combat all types of pathogens, and instead secrete preinflammatory cytokines, delaying the healing process.[6−8] While antibiotics have traditionally been the cornerstone of antibacterial treatment, the growing issue of antimicrobial resistance has significantly diminished their efficacy.[9,10] Hence, a nonantibiotic antibacterial strategy that can simultaneously modulate the immune environment holds promise for the efficient and specific treatment of bacterial-infected wounds.

Regarding nonantibiotic strategies, researchers have proposed diffusible antibacterial materials that release antimicrobial peptides,[11,12] as well as antibacterial coatings based on metal ions.[13,14] Additionally, contact-based bacterial-killing methods that leverage physical fields, such as light, sound, and electricity, are gaining attention. These methods align with the nature of bacterial infections, as bacteria tend to settle on surfaces before forming communities or biofilms.[15−17] Among these physical fields, electrical stimulation has attracted significant attention in the biomedical field due to its advantages, including cleanliness, environmental friendliness,

Received: July 9, 2025
Revised: August 31, 2025
Accepted: September 3, 2025
Published: September 11, 2025

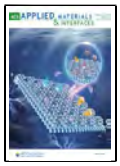

and wide applicability.[18,19] Our previous work involved constructing an array of carbon-doped titanium dioxide nanotubes, which demonstrated excellent antimicrobial capabilities postcharging by disrupting the bacterial respiratory chain.[20] Notably, antimicrobial materials inspired by electrical stimulation show considerable promise due to their high efficiency, minimal risk of drug resistance, and potential integration into smart medical devices for noninvasive treatment.[21] Despite the advantages of controllability, issues regarding the physicochemical and biofunctional properties of these materials must be addressed before they can be applied to wound healing. Currently, most antibacterial interfaces based on electrical stimulation are achieved using inorganic, rigid materials, which lack spatial adaptability when used as wound dressings. Hydrogels, however, are ideal for biological tissues due to their tissue-like mechanical properties, water content, excellent biocompatibility, flexibility, and versatility,[22−24] although their feasibility in delivering electrical stimulation has rarely been explored.[25] Thus, the development of flexible and conductive polymer hydrogels could enable effective electrical stimulation while offering antimicrobial benefits at the wound site, which is critical for wound care.[26,27] Even when conductive hydrogels are developed, these responsive materials often exhibit limitations when exposed to the complex immune microenvironment *in vivo*,[28−30] which can worsen wound condition by interacting with bacterial infections.[1,31] Therefore, an ideal wound care strategy based on electrical stimulation should also incorporate an immunomodulation functionality.

Coincidentally, electrical interactions can influence mammalian cell behavior in addition to bacterial infections.[32,33] Immune cells, including macrophages, are particularly electrically excitable due to specific ion channels that regulate their membrane potential in the presence of endogenous and exogenous electric fields. Electroactive materials such as graphene-based scaffolds have been developed to mediate electrical stimulation on macrophages, converting them from proinflammatory M1-type to anti-inflammatory M2-type, promoting angiogenesis, and activating fibroblast migration.[34,35] Therefore, it is reasonable to propose that a conductive hydrogel delivering proper electrical stimulation to the wound site could, on the one hand, directly combat infected bacteria and, on the other hand, modulate the immune system, thereby preventing infection and facilitating the transition from the inflammatory to the proliferative phase, ultimately accelerating the overall healing process. However, current electrostimulation research lacks integration of both antimicrobial and immunomodulatory effects, which could significantly enhance the treatment of complex wound repair.

Herein, a novel conductive and biocompatible hydrogel platform is developed to integrate antimicrobial activity and immune microenvironment modulation through electrical stimulation via simple charging. The acid-treated PEDOT:PSS hydrogel (AT-PP) is first prepared and then doped with manganese dioxide (MnO_2), resulting in the AT-PP@MnO_2 composite, which enhances the conductivity and doubles the capacitance to 0.28 mF cm^{-2} compared to AT-PP. After 15 min of energization at 0.8 V, AT-PP@MnO_2 exhibits exceptional electrochemical performance, achieving high and broad-spectrum bactericidal efficacy (up to 99%) by inducing an electron-transfer-driven intracellular ROS burst. When applied to an infected wound model, the electrical stimulation from the conductive hydrogel accelerates the healing process by killing bacteria (99%) and reversing macrophage polarization, thus regulating the imbalanced immune microenvironment. Benefiting from the outstanding dual modulatory effects of electrical stimulation, the wound healing rate in the AT-PP@MnO_2 group reaches 83% on day 7 and achieves near-complete healing by day 14, with no discernible toxicity concerns. This conductive hydrogel, which integrates wound healing functionality through bacterial intervention and immune modulation, provides an effective and safe physical strategy for developing wound dressings targeting infectious wounds.

2. MATERIALS AND METHODS

2.1. Materials and Chemicals. PEDOT:PSS suspension (Clevios PH1000, Heraeus), sulfuric acid (H_2SO_4, Sinopharm Chemical Reagent Co., Ltd.), ethanol (ETOH, General-reagent), potassium permanganate ($KMnO_4$, Sinopharm Chemical Reagent Co., Ltd.), and Milli-Q deionized water (18.2 MΩ) were used for all preparations.

2.2. Preparation of the Rechargeable Hydrogel Platform (AT-PP@MnO_2). The AT-PP hydrogel was synthesized as previously described.[36] Briefly, a PEDOT:PSS suspension (10.5 mg mL^{-1}) containing 0.1 mol L^{-1} of H_2SO_4 was sealed in a glass vial and heated at 90 °C for 3 h. The resultant hydrogels were purified by washing with deionized water several times. Subsequently, the hydrogels were immersed in a controlled concentration of H_2SO_4 solution for 12 h and washed to obtain an acid-treated PEDOT:PSS hydrogel (AT-PP). It is important to note that the concentration of H_2SO_4 should be increased gradually to avoid an irregular volume contraction of the hydrogels. For MnO_2 doping, AT-PP hydrogels were immersed in 5 mL of ethanol, followed by the addition of 3 mL of 0.1 M $KMnO_4$ solution and a coincubation for 30 min at room temperature. Hydrogels were thoroughly washed with deionized water, yielding AT-PP@MnO_2 hydrogels.

2.3. Characterization. The surface chemical states were analyzed by X-ray photoelectron spectroscopy (XPS, K-Alpha+, Thermo Fisher). Morphologies were examined via scanning electron microscopy (SEM, SU8010, Hitachi, Japan). Electrochemical properties were assessed using a CHI 660E electrochemical workstation (CHI 660E, Chenhua, China).

2.4. Adhesion Test. After the hydrogel samples were prepared, the adhesion experiments were carried out on the surfaces of nitrile gloves, glass slides, and fresh pig skin tissues, respectively. The state of stable adhesion was observed by placing the hydrogel samples upside down after slight contact with different surfaces, and images were recorded to analyze the adhesion effect.

2.5. Electrochemical Measurement. Hydrogel samples (1 × 1 cm^2) were used as the working electrode with platinum sheet counter electrodes and a saturated calomel electrode (SCE) reference. The electrolyte was phosphate-buffered saline (PBS, pH 7.2). Cyclic voltammetry (CV) measurements were conducted at 100 mV s^{-1} between −1.0 and 0 V. Galvanostatic charge−discharge (GCD) tests were performed at 2 mA cm^{-2}. Electrochemical impedance spectroscopy (EIS) was recorded from 0.01 Hz to 100 kHz with an amplitude of 10 mV.

2.6. *In Vitro* Charging Antibacterial Activity. Gram-negative *Escherichia coli* (ATCC 11775) and Gram-positive *Staphylococcus aureus* (ATCC 6538) were cultured in Luria−Bertani (LB) medium at 37 °C for 12 h. Bacterial suspensions (10^6 CFU mL^{-1}) were inoculated onto sterilized hydrogel samples and then electrically stimulated at 0.8 V for 15 min using an electrochemical workstation. Treated bacteria were serially diluted in PBS, plated on LB agar, and incubated for 24 h. Colony-forming units (CFU) were counted to determine bactericidal efficacy.

2.7. Live/Dead Bacterial Viability Assay. Bacterial viability was assessed using a Live/Dead *Bac*Light Bacterial Viability Kit (Beyotime, China). Briefly, 1 mL of staining solution was added to the treated bacterial and incubated for a duration of 20 min in the

https://doi.org/10.1021/acsami.5c13537
ACS Appl. Mater. Interfaces 2025, 17, 53232−53243

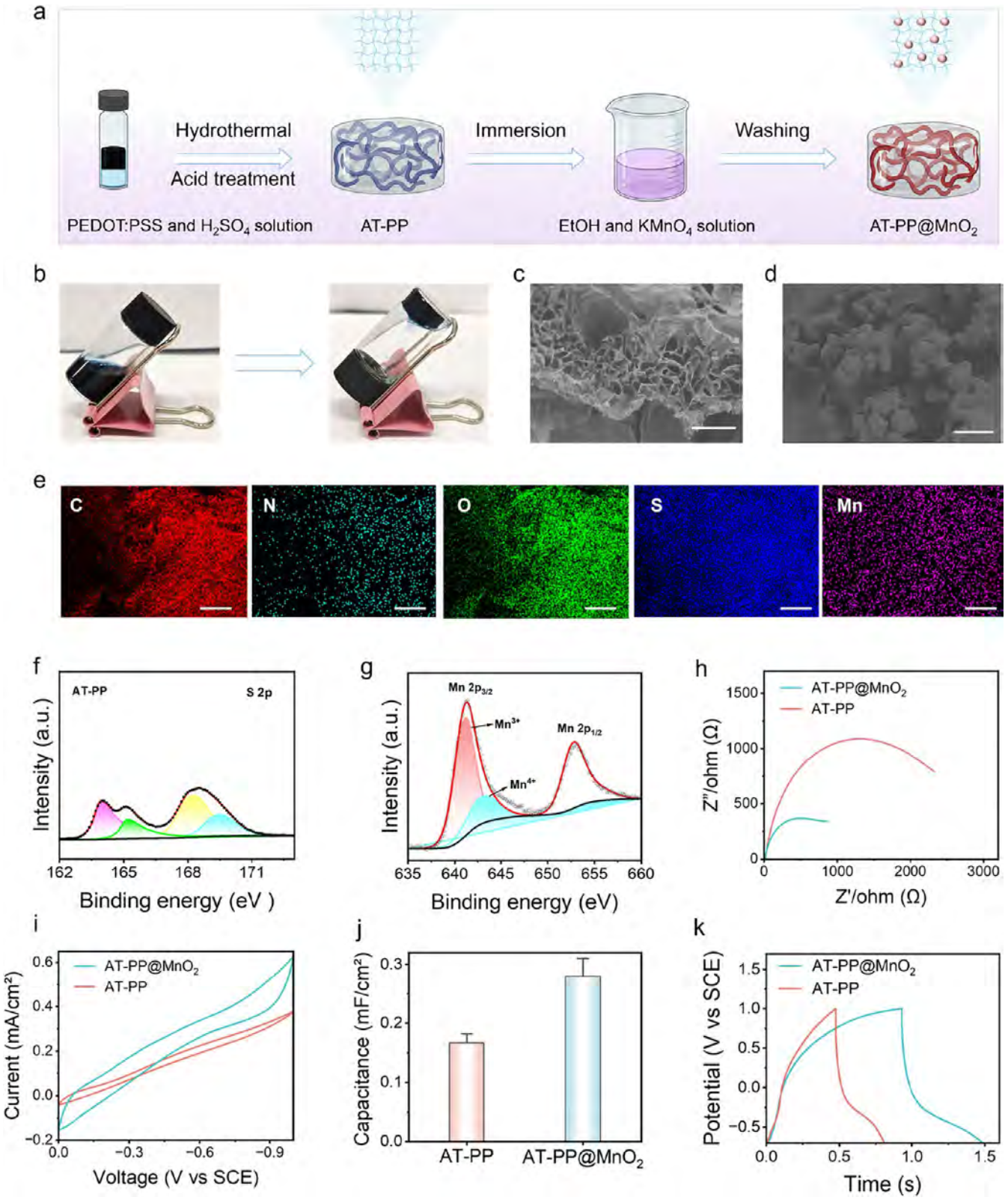

Figure 1. Preparation and characterization of the AT-PP@MnO_2 hydrogel. (a) Schematic illustration of the synthesis of AT-PP@MnO_2. (b) Representative optical images of the gelation progress of AT-PP@MnO_2. (c) SEM images of AT-PP@MnO_2. Scale bar: 100 μm. (d) SEM images of manganese dioxide nanoparticles. Scale bar: 2 μm. (e) Elemental mappings of AT-PP@MnO_2 by EDS. Scale bar: 100 μm. HR-XPS spectra of (f) S 2p of freeze-dried AT-PP and (g) Mn 2p of freeze-dried AT-PP@MnO_2 after charging. (h) EIS curves of AT-PP and AT-PP@MnO_2, respectively. (i) CV curves at a scanning rate of 100 mV s^{-1}. (j) Quantitative capacitances of AT-PP and AT-PP@MnO_2. (k) GCD curves of samples at a current density of 2 mA cm^{-2}.

https://doi.org/10.1021/acsami.5c13537
ACS Appl. Mater. Interfaces 2025, 17, 53232−53243

darkness. The samples were subsequently washed twice to remove excess staining solution, and the bacterial viability was visualized using a fluorescence microscope (FV3000, Olympus, Japan) with excitation wavelengths of 488/561 nm.

2.8. Observation of Bacterial Morphology. The morphology of bacteria was observed by using SEM (operated at 5 kV). Briefly, the bacterial samples were fixed in 2.5% glutaraldehyde for 6 h and subsequently dehydrated in a graded series of ethanol solutions (30, 50, 75, 90, and 100%) for 10 min at each step. The morphology of the bacteria was observed via SEM after gold sputter-coating.

2.9. Intracellular ROS Staining. The intracellular ROS levels of the bacteria were measured using a DCFH-DA fluorescence probe (Beyotime, China). In brief, DCFH-DA solution (10 μM) was added to the treated bacterial solution and incubated for 20 min in the dark. The fluorescence was subsequently observed by using inverted fluorescent microscopy with an excitation wavelength of 525 nm.

2.10. Measurement of Bacterial Membrane Potential. DiOC2(3) was used to assess the cell membrane potential of *E.coli* and *S. aureus*. In brief, the DiOC2(3) (30 μM) was added to the treated bacterial solution for 20 min at 37 °C. Subsequently, the bacterial potential was assessed via fluorescence images that were obtained through a Microplate Reader (SparkControl, Tecan, Switzerland).

2.11. Evaluation of Mn Ion Release. Mn ion release was quantified by ICP-OES (5800 ICP-OES, Agilent Technologies). Hydrogels (1 × 1 cm^2) were immersed in 5 mL of PBS (pH 7.4) at 37 °C. On day 20, supernatants were collected and analyzed (n = 3).

2.12. Evaluation of Cell Toxicity. Cell viability was evaluated using CCK-8 assays. HUVECs were cultured in DMEM medium (Gibco) supplemented with 10% fetal bovine serum and 1% penicillin/streptomycin. Sterilized samples were placed into 96-well plates and seeded with 5000 cells per well. The cells were incubated at 37 °C in a 5% CO_2 cell incubator for 1, 2, and 3 days, respectively. At each time point, CCK-8 staining solution (Beyotime, China) was added to the plates, and the relative viability was determined using a microplate reader at a wavelength of 490 nm. In addition, on day 3, the cells were stained using a Calcein/PI live−dead kit (Beyotime, China) and observed using a fluorescence microscope with excitation wavelengths of 488/561 nm to further assess cell viability.

2.13. Hemolysis Assay. The hemocompatibility of the samples was evaluated via a hemolysis assay. Sterilized samples were immersed in 0.9% saline solution for 24 h before being transferred to 1.5 mL EP tubes. A mixture of 0.9 mL of saline solution and 0.1 mL of diluted mouse blood solution was added to the tubes and incubated at 37 °C for 3 h. The mixture solution was centrifuged at 1000 rpm for 5 min, and the relative hemolysis rate was determined using a microplate reader at a wavelength of 545 nm. Hemolysis rate was calculated as

$$\text{hemolysis (\%)} = (A_{\text{sample}} - A_{\text{negative}})/(A_{\text{positive}} - A_{\text{negative}}) \times 100$$

where A represents the absorbance value.

2.14. Infectious Wound Treatment. The ability of *in vivo* bacterial eradication and immune modulation by the chargeable hydrogel was evaluated by using a *S. aureus*-infected wound model. All animal experiments were approved by the Institutional Animal Care and Use Committee of Tongji University. The 8-week-old male BALB/c mice with an average weight of 200 g were randomly assigned to one of four groups: healthy, control, hydrogel treatment group without charging (AT-PP@MnO_2 (−)), and hydrogel treatment group with charging (AT-PP@MnO_2 (+)) (n = 6). Following anesthesia, a full-thickness wound with a diameter of 10 mm was created on the back of each mouse using a sterile skin punch, and 0.1 mL of bacterial solution (4 × 10^8 CFU mL^{-1}) was dropped onto the wound site. After infection for 24 h, the control group remained untreated, while AT-PP@MnO_2 (−) was covered with a conductive hydrogel without initiating electrical stimulation. The AT-PP@MnO_2 (+) was covered with conductive hydrogels and subjected to electrical stimulation (0.8 V) for 15 min every 2 days. During the 15 min electrical stimulation, the mice were gently restrained using a commercial animal restrainer designed for small rodents, which allows immobilization without causing pain or stress. Photographs were taken at various time points (day 0, 3, 7, 10, and 14) to document wound size variation. The relative closure rate (%) was calculated according to the following equation:

$$\text{relative closure rate (\%)} = (A_0 - A_t)/A_0 \times 100$$

where A_0 represents the initial wound area at day 0 and A_t is the wound area measured at the indicated time points. The wound area was quantified based on digital photographs using ImageJ software.

On days 5 and 14, the wounds were harvested to assess the amounts of residual bacteria in different groups. Besides, the hematoxylin and eosin (H&E) staining, Masson staining, and immunofluorescence staining for CD163 and INOS were conducted to evaluate the state of wound repair and inflammation. The major organs of mice were also collected to conduct H&E staining for evaluating the *in vivo* biosafety of AT-PP@MnO_2.

2.15. Statistical Analysis. Data were presented as the mean ± SD with *, **, and *** denoting $p < 0.05$, $p < 0.01$, and $p < 0.001$, respectively, in Origin 2025 software.

3. RESULTS AND DISCUSSION

3.1. Preparation and Characterization of the Chargeable Hydrogel (AT-PP@MnO_2). Conductivity and capacitance are key factors in the design of chargeable hydrogels.[37,38] We first synthesize conductive AT-PP by treating commercial PEDOT:PSS with acid (Figure 1a). MnO_2 nanoparticles are then *in situ* incorporated to facilitate transient charge storage and release, resulting in the formation of AT-PP@MnO_2. Representative optical images illustrate the gelation process of AT-PP@MnO_2, which exhibits a dark blue color, confirming the feasibility of the synthetic method (Figure 1b). The synthesized hydrogel is observed to have micrometer-scale dimensions, as shown in scanning electron microscopy (SEM) images (Figure 1c). The successful incorporation of MnO_2 nanoparticles is evident (Figure 1d), acting as an electron collector for charge storage and release, thereby enhancing the overall conductivity and capacitance of AT-PP@MnO_2. The presence of C, N, O, S, and Mn elements, confirmed by energy-dispersive spectroscopy (EDS), supports the successful preparation of AT-PP@MnO_2 and the incorporation of MnO_2 (Figures 1e and S1). Furthermore, in the high-resolution (HR) S 2p X-ray photoelectron spectroscopy (XPS), the intensity ratios of the AT-PP at 168 and 164 eV are significantly lower than those of PEDOT:PSS (Figures 1f and S2). The peak at 168 eV is attributed to the S atoms of the polystyrene sulfonate (PSS) chain, and the two peaks at 164 and 165 eV are linked to the S atoms of the PEDOT:PSS chain.[39,40] This indicates that the PSS is partially removed from the PEDOT:PSS complexes,[36] thereby validating the hypothesis that the acid treatment can enhance electrochemical performance. Concurrently, XPS spectra of Mn 2p are collected before and after electrical stimulation (Figures 1g and S3). The Mn^{4+} peak at 643.2 eV partially decreases after charging, while the Mn^{3+} peak at 642.1 eV increases correspondingly. This shift indicates a reversible Mn^{4+} to Mn^{3+} redox transition during charging, confirming that MnO_2 actively participates in the charge storage/release process, thereby further supporting the augmentation of electrochemical performance.[41] To preliminarily evaluate the practical applicability of the AT-PP@MnO_2 hydrogel as a wound dressing, we assess its adhesive performance on various clinically relevant substrates, including nitrile gloves, glass surfaces, and porcine skin tissues (Figure S4). The results indicate satisfactory adhesion capability across

https://doi.org/10.1021/acsami.5c13537
ACS Appl. Mater. Interfaces 2025, 17, 53232−53243

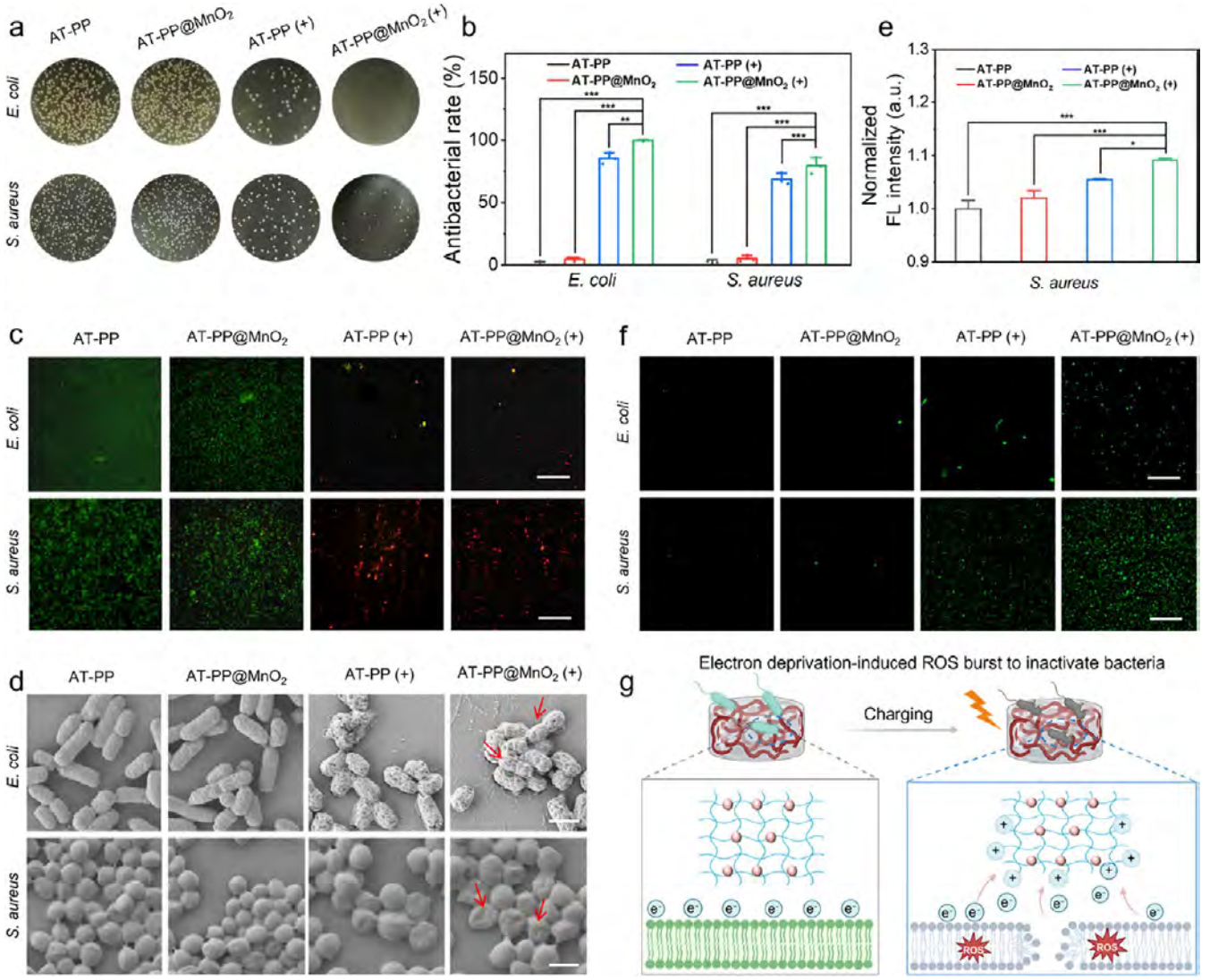

Figure 2. Charging to eradicate bacteria by AT-PP@MnO_2 and the underlying mechanism. (a) Representative images of *E. coli* and *S. aureus* colonies. (b) Corresponding quantitative analysis of antibacterial rates on *E. coli* and *S. aureus*. (c) Live/dead (green/red) fluorescence staining images of *E. coli* and *S. aureus* upon various groups. Scale bar: 50 μm. (d) Representative SEM images of bacteria upon different treatments to characterize morphological changes. Scale bar: 1 μm. (e) Variation of bacterial membrane potential after various treatments. (f) Intracellular ROS evaluation of *E. coli* and *S. aureus* using the DCFH-DA probe. Scale bar: 50 μm. (g) Schematic illustration of the antimicrobial mechanism of AT-PP@MnO_2: Charging drives electron transfer from bacteria to AT-PP@MnO_2 and subsequently induces an intracellular ROS burst to damage the bacterial structure. Data are presented as the mean ± SD with *, **, and *** denoting $p < 0.05$, $p < 0.01$, and $p < 0.001$, respectively.

different interfaces, especially notable on biological tissue surfaces, suggesting potential for stable interface adherence during clinical applications.

The electrochemical performance of AT-PP@MnO_2 is then evaluated by using an electrochemical workstation. Electrochemical impedance spectroscopy (EIS) shows that the impedance of AT-PP@MnO_2 is lower than that of AT-PP (Figure 1h), suggesting a significant reduction in interfacial charge transfer resistance and more efficient ion/electron transport. This improvement is further confirmed by cyclic voltammetry (CV) and galvanostatic charge−discharge (GCD) tests. The CV curves of AT-PP@MnO_2 display a substantially higher current density compared to that of AT-PP (Figure 1i), indicating that the introduction of MnO_2 nanoparticles enhances the capacitive properties. The capacitance of AT-PP@MnO_2 is calculated to be 0.28 mF cm^{-2}, nearly twice as high as that of AT-PP (Figure 1j). This enhancement is primarily attributed to the charge storage capacity arising from the valence transition of MnO_2. Additionally, the GCD profile at a current density of 2 mA cm^{-2} demonstrates a significantly prolonged charge release time for AT-PP@MnO_2, highlighting its superior charge storage and release capabilities following the *in situ* formation of MnO_2 nanoparticles (Figure 1k). These results indicate the successful preparation of conductive AT-PP@MnO_2 hydrogel, with MnO_2 playing a pivotal role in boosting its electrochemical performance.

3.2. Charging-Induced Antibacterial Activity. The antimicrobial activity of conductive AT-PP@MnO_2 via an easy-to-operate charging process is then evaluated by colony-forming units (CFU) counting with Gram-negative *Escherichia coli* (*E. coli*) and Gram-positive *Staphylococcus aureus* (*S. aureus*) as model strains. Bacteria in the rapid growth phase are first inoculated onto samples, which are then charged. After

https://doi.org/10.1021/acsami.5c13537
ACS Appl. Mater. Interfaces 2025, 17, 53232−53243

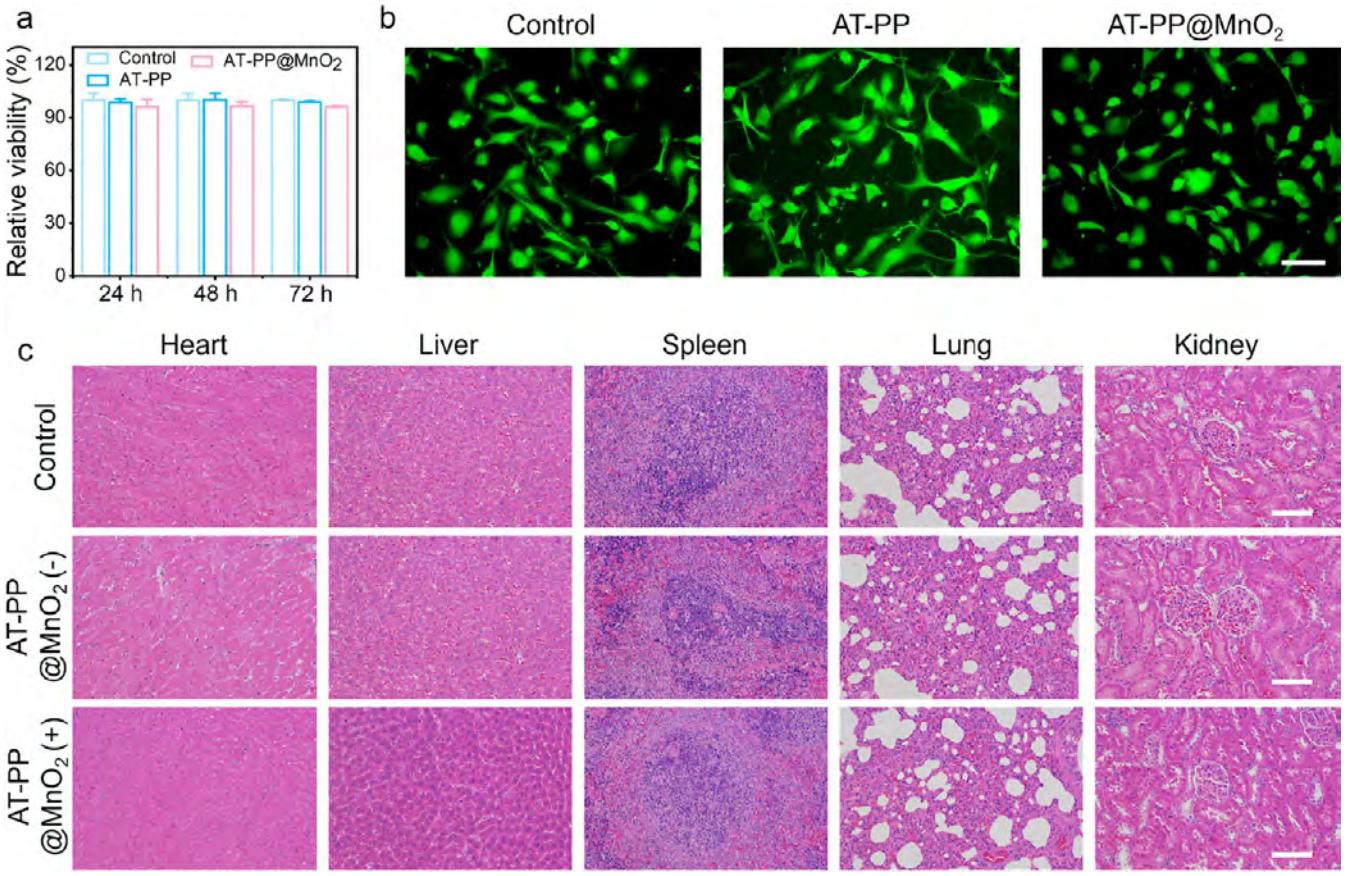

Figure 3. Safety assessment of AT-PP@MnO_2. (a) Relative viability of HUVECs after different treatments for 24, 48, and 72 h. (b) Representative fluorescence images of HUVECs stained with Calcein-AM/PI for marking live cells (green) and dead cells (red). Scale bar: 200 μm. (c) Representative images of H&E staining of major organs, including heart, liver, spleen, lungs, and kidneys, treated with different groups. Scale bar: 100 μm. Data are presented as the mean ± SD.

charging for 15 min at a potential as low as 0.8 V, AT-PP (+), with "(+)" denoting the electrically charged state, reduces *E. coli* and *S. aureus* by 85 and 68%, respectively (Figure 2a,b). This tentatively demonstrates the rapid sterilization ability of AT-PP during the charging process. Specially, AT-PP@MnO_2 (+) hydrogel achieves substantially improved antibacterial ability, killing nearly 100% of the *E. coli*, which is attributed to the enhanced conductivity and capacitance of MnO_2 nanoparticles. The real-time viability of treated bacteria is marked by Calcein-AM/PI fluorescence staining, with red dots indicating dead bacteria and green representing live ones. As shown in Figure 2c, a few red-stained dead bacteria could be observed on pristine AT-PP and AT-PP@MnO_2, suggesting that uncharged hydrogels do not adversely affect bacterial viability. In contrast, substantially improved intensity of red fluorescence appears in the charging group of AT-PP (+) and AT-PP@MnO_2 (+), demonstrating more severe membrane damage and bacterial death, corresponding with the results from CFU counting.

3.3. Underlying Antibacterial Mechanism of AT-PP@MnO_2 Hydrogel upon Charging. As the mechanism of live/dead staining is based on the principle that lipophilic green dye Calcein-AM easily penetrates the cell membranes of all bacteria, whereas the red dye propidium iodide (PI) could only stain bacteria with damaged cell membranes, the blossom red dots in charging groups signify an intervention on membrane integrity by charging (Figure 2c). This could be further confirmed by SEM observations (Figure 2d) that bacteria in uncharged groups exhibit intact cell membranes and normal morphology, whereas they show significant membrane pores and morphological shrinkage (red arrows) after charging.

The above membrane disruption is further measured by comparing the change of membrane potential after charging to further uncover antibacterial mechanisms of chargeable AT-PP@MnO_2. The elevated fluorescence intensity in charged groups indicates a decreased membrane potential (Figures 2e and S5). AT-PP@MnO_2 (+) exhibits the largest decrease in the membrane potential, demonstrating the most severe electron loss. The intracellular ROS levels of different groups are measured using the fluorescent probe DCFH-DA. The strongest green fluorescence detected in the AT-PP@MnO_2 (+) group supports the violent interference caused by depolarization (Figure 2f). Besides, ICP-OES analysis shows a cumulative Mn ion concentration of 50 ng mL^{-1} in the supernatant after 20 days, indicating minimal Mn ion leaching from AT-PP@MnO_2 under physiological conditions (Figure S6). Given this low level and the negligible antibacterial effect without charging, the rapid killing observed upon electrical stimulation is unlikely to originate from ion release. Based on the above experimental results, a possible charging bactericidal mechanism is proposed as follows. The generated positive charges within AT-PP@MnO_2 (+) during the charging process may interact with the negatively charged bacterial membrane to deprive electrons. The further loss of electrons disrupts redox homeostasis within the bacteria, leading to an intra-

https://doi.org/10.1021/acsami.5c13537
ACS Appl. Mater. Interfaces 2025, 17, 53232−53243

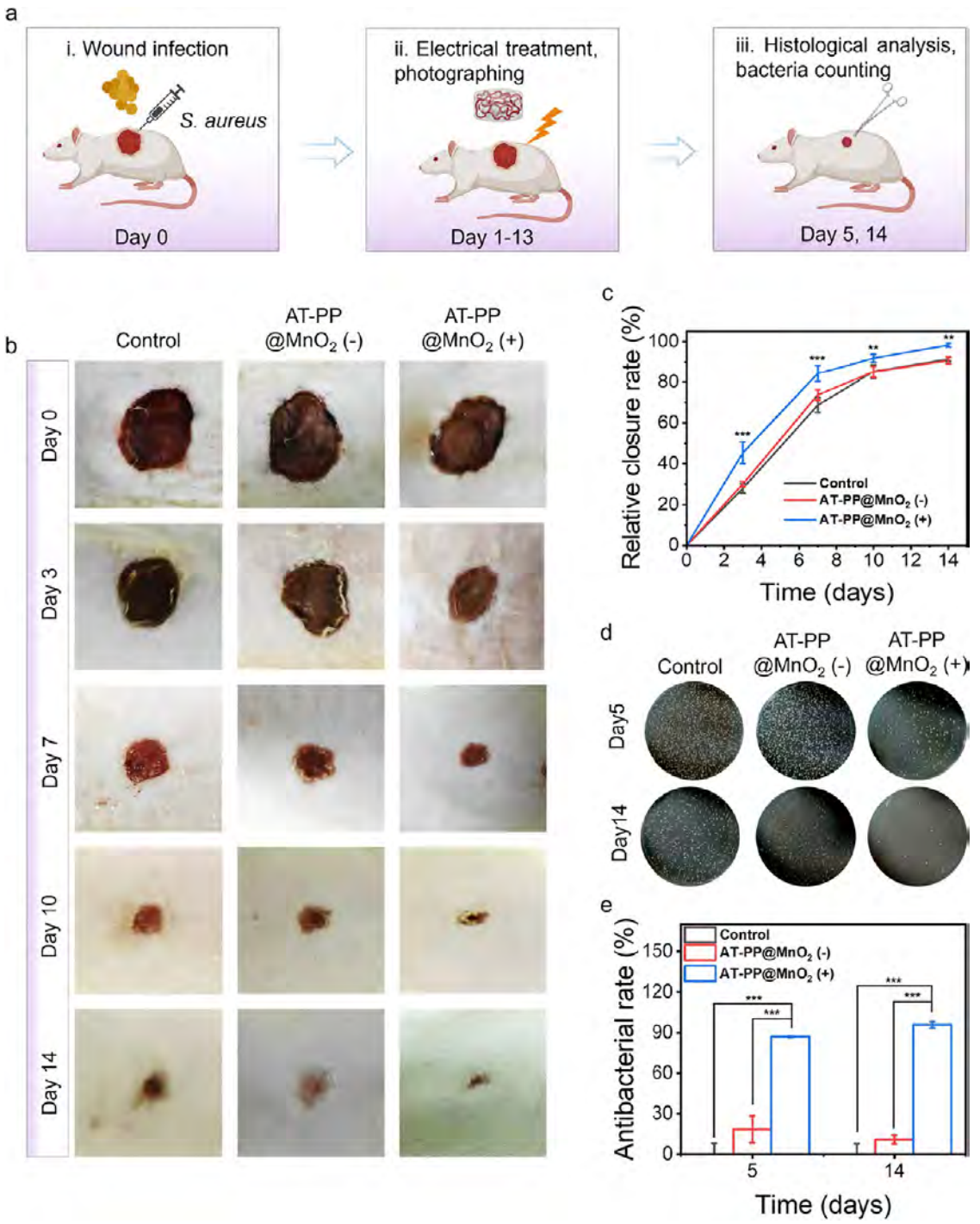

Figure 4. *In vivo* charging disinfection ability of AT-PP@MnO_2. (a) Schematic illustration depicting the *in vivo* experimental setup. (b) Representative photographs to record the healing process of infected wounds. (c) Relative wound closure rate measured from day 1 to day 14 in different groups ($n = 6$). (d) Representative photographs of residual bacteria after various treatments on days 5 and 14. (e) Quantitative analysis of antibacterial efficiency on days 5 and 14. Data are presented as the mean ± SD with ** and *** denoting $p < 0.01$ and $p < 0.001$, respectively.

cellular ROS burst. This burst damages the bacterial structure and ultimately induces bacterial death (Figure 2g).

3.4. Safety Assessment of AT-PP@MnO_2. Biosafety evaluation is crucial for assessing the potential of biomaterials in practical applications. Human Umbilical Vein Endothelial Cells (HUVECs) play a crucial role in wound repair and are selected to evaluate the biotoxicity of AT-PP@MnO_2 using the typical CCK-8 assay. After culture with HUVECs for 24, 48, and 72 h, indiscernible cell toxicity could be measured with relative cell survival exceeding 90%, indicating the good cytocompatibility of AT-PP@MnO_2 (Figure 3a). Cell viability is further assessed by live/dead fluorescence staining. HUVECs in the group of AT-PP@MnO_2 maintain good growth patterns, and few red-stained dead cells are observed compared with the control group, further demonstrating the outstanding biocompatibility of AT-PP@MnO_2 (Figure 3b). The hemocompatibility of AT-PP@MnO_2 is also evaluated using a hemolysis test (Figure S7). The hemolysis rate is less than 4% in all

https://doi.org/10.1021/acsami.5c13537
ACS Appl. Mater. Interfaces 2025, 17, 53232−53243

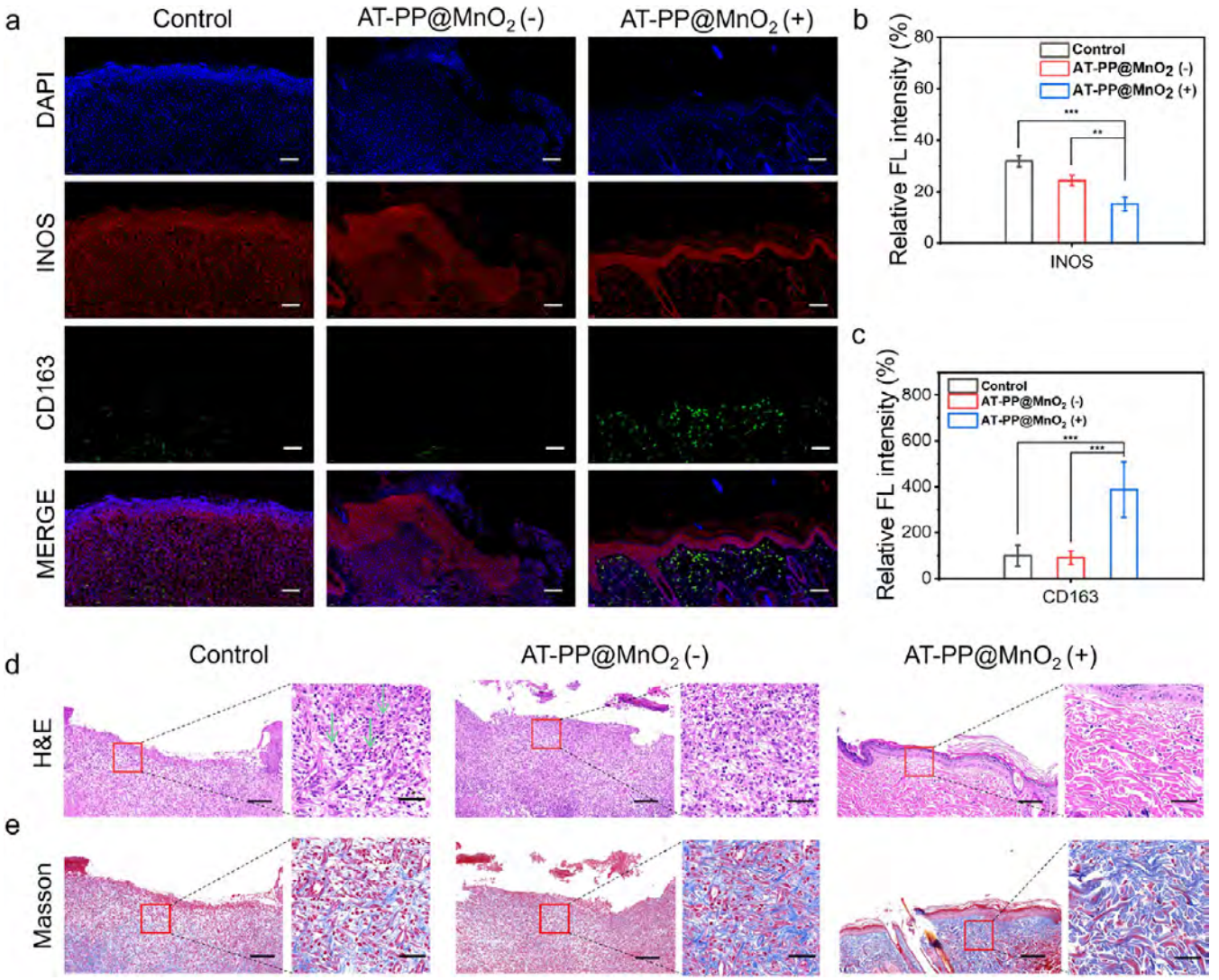

Figure 5. Charging to evoke immune modulation by AT-PP@MnO_2. (a) Representative immunofluorescence images of INOS (M1) and CD163 (M2) staining of wound tissues after various treatments on day 5. Scale bar: 100 μm. Quantitative analysis of relative fluorescence intensity of (b) INOS, and (c) CD163 staining. Representative (left) and magnified (right) images of (d) H&E, and (e) Masson staining of infected wound after different treatments on day 5. Scale bar: 200 μm (left) and 50 μm (right). Data are presented as the mean ± SD with *, **, and *** denoting $p < 0.05$, $p < 0.01$, and $p < 0.001$, respectively.

groups, within the internationally defined safety limit.[42] In addition to *in vitro* cell experiments, we also evaluate the *in vivo* biotoxicity of AT-PP@MnO_2 on mice. The H&E slices of mice's major organs present that both the charging and noncharging groups of AT-PP@MnO_2 generate indistinguishable toxicity, proving the good biocompatibility *in vivo* as well (Figure 3c). The results of the H&E-stained section show that the histological structure of each major organ (heart, liver, spleen, lung, and kidney) remains intact without significant inflammation, necrosis, or other pathological injury in the AT-PP@MnO_2 (+) groups. This suggests that the AT-PP@MnO_2 does not show a significant toxic response to the different organs of the mice at the dosages and conditions evaluated. PEDOT:PSS is widely reported to be a conductive polymer with good biocompatibility for use as a bioactive material,[43,44] and ultralow voltage electrical stimulation in this work does not induce a strong Faraday electrode response in the culture medium and does not produce toxic substances.[45]

3.5. *In Vivo* Charging Disinfection by AT-PP@MnO_2. Bacterial infections can cause persistent inflammation, tissue damage, and delayed healing during the wound healing process, and in severe cases can even lead to the spread of infection and chronic wounds. Effective bacterial inactivation not only reduces the inflammatory response and tissue necrosis but also promotes cell proliferation and neovascularization, thereby accelerating wound repair and improving the quality of healing. The remarkable bactericidal ability and minimal biosafety of AT-PP@MnO_2 encourage the construction of an infectious wound model to investigate *in vivo* antibacterial efficiency (Figure 4a). As shown in Figure 4b, obviously accelerated wound healing could be observed in the AT-PP@MnO_2 (+) group compared with the control and AT-PP@MnO_2 (−) group. The quantified results show that the wound closure rate of the AT-PP@MnO_2 (+) group is 43% on day 3, which is significantly higher than that of the control (23%) and AT-PP@MnO_2 (−) groups (24%) (Figure 4c). On day 10, wounds in the AT-PP@MnO_2 (+) group exhibit nearly complete healing, while control and AT-PP@MnO_2 (−) groups have significant residual damage. This suggests that charged AT-PP@MnO_2 is effective in promoting wound

https://doi.org/10.1021/acsami.5c13537
ACS Appl. Mater. Interfaces 2025, 17, 53232−53243

healing, particularly in the early stages of repair. Furthermore, residual bacteria at wounds of different groups are measured to evaluate the *in vivo* bactericidal efficiency of AT-PP@MnO_2. It could be clearly seen that the bacterial number in the group of AT-PP@MnO_2 (+) is significantly lower than that in the group of control and AT-PP@MnO_2 (−) (Figure 4d). The quantitative analysis indicates that charged AT-PP@MnO_2 could rapidly inactivate over 99% bacteria on day 14, while the group of control and AT-PP@MnO_2 (−) shows negligible antibacterial activity (Figure 4e). This demonstrates the crucial role of charging in initiating bacterial eradication and the outstanding *in vivo* bactericidal ability of charged AT-PP@MnO_2.

3.6. Electrical Stimulation-Driven Immune Modulation by AT-PP@MnO_2. Wound healing involves four sequential and overlapping phases: hemostasis, inflammation, proliferation, and remodeling.[46] Persistent bacterial infection triggers sustained immune responses, hindering progression in the inflammatory phase and impeding entry into the proliferative repair phase.[47] In addition to timely eradicating invasive pathogens, reprogramming the off-balance immune microenvironment at the wound site is also crucial for promoting wound repair. As a critical regulatory factor in wound healing, macrophages control the inflammatory response stages through various sequential biological activities.[48] Electrical stimulation driven by the charged AT-PP@MnO_2 is expected to modulate macrophage polarization and attenuate proinflammatory effects. To determine the effect of the conductive hydrogel platform on macrophage polarization, we perform immunofluorescence staining on macrophages. As shown in Figure 5a,b, a relatively weaker fluorescence intensity of INOS is observed in the group of AT-PP@MnO_2 (+), indicating the lower number of M1 macrophages. In addition, significantly enhanced levels of CD163 expression (M2 macrophages) can also be observed in the group of AT-PP@MnO_2 (+) compared with other groups (Figure 5a,c). These findings suggest that electrical stimulation modulates the immune response toward a reparative phenotype, thereby contributing to improved wound healing.

The formation of epidermal dermis and collagen deposition is further evaluated by histologic analysis, including hematoxylin and eosin (H&E) and Masson staining. On day 5, a substantial infiltration of inflammatory cells (black arrows in Figure 5d) could be observed in both the control and AT-PP@MnO_2 (−) groups, in comparison to the reduced presence of inflammatory cells in the AT-PP@MnO_2 (+) group (Figure 5d). This suggests that the inflammatory response is progressively subsiding and the tissue repair process is progressing to the subsequent phase. By day 14, mild inflammation persists, although basic epithelial and dermal structures form in the control and AT-PP@MnO_2 (−) and AT-PP@MnO_2 (−) groups (Figure S8). Notably, the AT-PP@MnO_2 (+) group exhibits the formation of a mature and dense epidermis with a substantial number of hair follicles (yellow arrows in Figure S8), indicating a more developed and functional skin. This demonstrates that charged AT-PP@MnO_2 effectively promotes dermal tissue regeneration. Collagen, a principal component of the extracellular matrix, plays a pivotal role in wound cell proliferation and migration through its synthesis and organization. To assess the collagen content in regenerated tissues, Masson staining is employed. On days 5 and 14, the AT-PP@MnO_2 (+) group exhibits a denser mesh of fibers, while the control and AT-PP@MnO_2 (−) groups exhibit fewer and more loosely arranged collagen fibers (Figures 5e and S8). Together, these results confirm that charged AT-PP@MnO_2 accelerates wound repair by both eradicating pathogens and alleviating local inflammation.

4. DISCUSSION

In this study, we present an innovative rechargeable conductive hydrogel platform that combines electrical stimulation-driven dual modulatory effects, i.e., efficient bacterial inactivation and immune microenvironment remodeling. By doping MnO_2 nanoparticles into acid-treated PEDOT:PSS hydrogels (AT-PP), we successfully construct a system capable of storing and releasing electrical charges. The system achieves up to 99% bacterial inactivation in only 15 min at 0.8 V, demonstrating its excellent electrochemical performance and strong antimicrobial capability. MnO_2 doping in AT-PP is essential for enhancing the electrochemical and biological functions. It improves charge storage and transfer, boosting antibacterial efficacy and enabling a stronger ROS burst. The *in vivo* results also confirm that MnO_2 promotes faster wound healing and immune modulation with a shift from M1 to M2 macrophage markers. These results demonstrate that MnO_2 doping is crucial for achieving robust antibacterial action and immune reprogramming under low-voltage stimulation, which AT-PP alone cannot fully provide. Compared with conventional antibiotic therapy and other physically driven antimicrobial strategies, AT-PP@MnO_2 provides a noninvasive electrochemical drive that not only avoids the problem of drug resistance but also produces a remarkable antimicrobial effect through the intracellular ROS burst induced by electron transfer. In addition to these effects, we also explore the underlying mechanisms of bacterial inactivation and immune modulation, broadening the application of electrical charging for wound healing.

Our findings indicate that electrical stimulation is highly effective in attenuating bacterial viability by disrupting the membrane and elevating the intracellular ROS. Bacterial membranes typically maintain a negative resting membrane potential, with the inside of the cell being more negative relative to the outside. When exposed to the positively charged hydrogel, the interface potential exerts a strong attraction to intracellular electrons, resulting in a significant membrane depolarization. This depolarization impairs bacterial growth, metabolism, and stress response, which is directly reflected by the fluctuation of intracellular ROS levels.[49] The ROS burst disrupts the bacterial membrane, leading to bacterial death.[50] This mechanism explains the high bactericidal efficiency observed in our hydrogel system, demonstrating that electrical stimulation is an effective strategy for eradicating pathogens in infected wounds.

Moreover, the proposed platform demonstrates the ability to remodel the traumatic immune microenvironment effectively. Immune modulation plays a critical role in wound healing. M1 macrophages are known for secreting proinflammatory cytokines such as TNF-α and IL-1β, thereby contributing to prolonged inflammation that hinders wound repair. In contrast, M2 macrophages produce higher levels of anti-inflammatory cytokines, including IL-10, TGF-β, and VEGF, which promote tissue regeneration.[51] The ability of electrical stimulation to reprogram macrophage polarization from M1 to M2 thus provides an essential mechanism for accelerating wound healing. By facilitating this phenotypic shift, electrical stimulation not only alleviates inflammation but also creates

https://doi.org/10.1021/acsami.5c13537
ACS Appl. Mater. Interfaces 2025, 17, 53232−53243

a favorable microenvironment for fibroblast migration, angiogenesis, and collagen deposition.

The bacterial killing and immunomodulation processes together pave the way for wound healing. Building on this, we propose a possible mechanism underlying the therapeutic efficacy of electrical stimulation.[52] First, electrical stimulation effectively eliminates invading pathogens, thereby reducing local infections and preventing exacerbated inflammation. Second, electrostimulation rebalances the wound immune microenvironment by reprogramming macrophages from the proinflammatory M1 phenotype to the reparative M2 phenotype, which further promotes fibroblast proliferation, neovascularization, and collagen deposition. These synergistic effects enable rapid and efficient wound healing, with collagen formation serving as a key marker. In this work, collagen formation and extracellular matrix remodeling are significantly amplified by electrical stimulation, which in turn optimizes the immune response and facilitates the key cellular processes necessary for effective wound healing. While our current animal experiments are conducted over 2 weeks, this duration remains meaningful as it captures both the inflammatory and proliferative phases of wound healing, during which macrophage phenotype switching plays a key role. Previous studies have demonstrated that interventions that successfully reprogram macrophages within this time frame often lead to favorable long-term tissue outcomes, including reduced scarring and improved remodeling.[6,7] Therefore, our current data not only provide valuable short-term insights but also offer indicative evidence of beneficial long-term immune regulation.

In conclusion, our study demonstrates that electrical stimulation through a chargeable hydrogel platform provides a dual modulatory effect, combining bacterial inactivation with immune modulation to accelerate tissue remodeling and wound healing. This dual approach offers a promising therapeutic strategy for treating infected wounds. While the direct current used in this work may seem cumbersome, recent studies have shown the feasibility of integrating conductive biomaterials with wireless charging modules for antibacterial therapy and wound monitoring.[53,54] Therefore, our chargeable hydrogel platform could be further developed into a clinically practical solution by coupling it with wireless electronics, providing a more convenient and efficient approach for wound care applications.

5. CONCLUSIONS

Infectious wounds face a complex pathological microenvironment characterized by notorious pathogens and an imbalanced immune system. Popular nanotherapies initiated by phototherapy, ultrasound, and enzyme-like catalysis to generate lethal ROS have received wide attention in overcoming antimicrobial resistance. Regrettably, their applications in wound healing are somehow hindered by toxicity and the inability to reconstruct an imbalanced immune microenvironment. Electrical stimulation, as a safe and easy-to-operate technique, has been demonstrated to achieve efficient bacterial inactivation and has shown potential in immune modulation. However, current research still lacks a soft, biocompatible platform that integrates electrical stimulation to facilitate the healing of infectious wounds. In this work, we develop a rechargeable conductive hydrogel (AT-PP@MnO_2) that integrates antibacterial activity with immune modulation under safe, low-voltage stimulation. This soft and biocompatible platform eradicates invasive pathogens through electron-transfer-induced ROS generation and simultaneously reprograms macrophage polarization to favor tissue repair. By combining these dual modulatory effects, the system accelerates wound healing while maintaining biosafety. Our findings highlight a new physical strategy for designing multifunctional dressings that not only control infection but also reshape the immune microenvironment, offering promising implications for next-generation wound care and regenerative medicine.

ASSOCIATED CONTENT

Supporting Information

The Supporting Information is available free of charge at https://pubs.acs.org/doi/10.1021/acsami.5c13537.

Elemental mappings of AT-PP by EDS (Figure S1); HR-XPS spectra of S 2p for freeze-dried PEDOT:PSS (Figure S2); HR-XPS spectra of Mn 2p of freeze-dried AT-PP@MnO_2 before charging (Figure S3); adhesive performance evaluation of AT-PP@MnO_2 on nitrile gloves, glass, and porcine skin (Figure S4); variation of bacterial membrane potential for *E. coli* after various treatments (Figure S5); cumulative Mn ion release of AT-PP@MnO_2 in PBS solution (pH = 7.4) compared to other similar works (Figure S6); hemolytic rate of red blood cells after incubation with different samples (Figure S7); representative and magnified images of H&E, and Masson staining of infected wounds after different treatments on day 14 (Figure S8) (PDF)

AUTHOR INFORMATION

Corresponding Author

Guomin Wang − *State Key Laboratory of Cardiovascular Diseases and Medical Innovation Center, Shanghai East Hospital, School of Medicine, Tongji University, Shanghai 200070, China;* orcid.org/0000-0003-2707-7051; Email: wangguominhi@gmail.com

Authors

Yiheng Tang − *State Key Laboratory of Cardiovascular Diseases and Medical Innovation Center, Shanghai East Hospital, School of Medicine, Tongji University, Shanghai 200070, China;* orcid.org/0009-0008-8093-057X

Guopeng Xu − *State Key Laboratory of Cardiovascular Diseases and Medical Innovation Center, Shanghai East Hospital, School of Medicine, Tongji University, Shanghai 200070, China;* orcid.org/0009-0005-6742-5104

Jing Liu − *Tianjin Key Laboratory of Biomaterial Research, Institute of Biomedical Engineering, Chinese Academy of Medical Sciences and Peking Union Medical College, Tianjin 300192, China*

Jiezhou Wu − *State Key Laboratory of Cardiovascular Diseases and Medical Innovation Center, Shanghai East Hospital, School of Medicine, Tongji University, Shanghai 200070, China;* orcid.org/0009-0008-2023-8389

Jingyang Fang − *State Key Laboratory of Cardiovascular Diseases and Medical Innovation Center, Shanghai East Hospital, School of Medicine, Tongji University, Shanghai 200070, China;* orcid.org/0009-0003-5314-4876

Shengji Gu − *State Key Laboratory of Cardiovascular Diseases and Medical Innovation Center, Shanghai East Hospital,*

School of Medicine, Tongji University, Shanghai 200070, China; orcid.org/0009-0001-0890-7518

Wenyan Zhang − *State Key Laboratory of Cardiovascular Diseases and Medical Innovation Center, Shanghai East Hospital, School of Medicine, Tongji University, Shanghai 200070, China*

Wenkun Zhang − *State Key Laboratory of Cardiovascular Diseases and Medical Innovation Center, Shanghai East Hospital, School of Medicine, Tongji University, Shanghai 200070, China*

Junfeng Hu − *State Key Laboratory of Cardiovascular Diseases and Medical Innovation Center, Shanghai East Hospital, School of Medicine, Tongji University, Shanghai 200070, China*

Paul K. Chu − *Department of Physics, Department of Materials Science and Engineering, and Department of Biomedical Engineering, City University of Hong Kong, Kowloon 999077, Hong Kong;* orcid.org/0000-0002-5581-4883

Jianzhong Du − *Department of Polymeric Materials, School of Materials Science and Engineering, Tongji University, Shanghai 201804, China;* orcid.org/0000-0003-1889-5669

Complete contact information is available at: https://pubs.acs.org/10.1021/acsami.5c13537

Author Contributions

[⊥]Y.T., G.X., and J.L. contributed equally to this work.

Notes

The authors declare no competing financial interest.

■ ACKNOWLEDGMENTS

This work was supported by the National Key Research and Development Program of China (2023YFB3809900 and 2023YFB3809901), the National Natural Science Foundation of China (82302382), the Shanghai Natural Science Foundation (23ZR1467100), and the CAMS Innovation Fund for Medical Sciences (No. 2022-I2M-1-023).

■ REFERENCES

(1) Uberoi, A.; McCready-Vangi, A.; Grice, E. A. The wound microbiota: microbial mechanisms of impaired wound healing and infection. *Nat. Rev. Microbiol.* **2024**, *22* (8), 507−521.

(2) Harris-Tryon, T. A.; Grice, E. A. Microbiota and maintenance of skin barrier function. *Science* **2022**, *376* (6596), 940−945.

(3) Sani, E. S.; Xu, C.; Wang, C.; Song, Y.; Min, J.; Tu, J.; Solomon, S. A.; Li, J.; Banks, J. L.; Armstrong, D. G.; Gao, W. A stretchable wireless wearable bioelectronic system for multiplexed monitoring and combination treatment of infected chronic wounds. *Sci. Adv.* **2023**, *9* (12), No. eadf7388.

(4) Cai, Y.; Chen, K.; Liu, C.; Qu, X. Harnessing strategies for enhancing diabetic wound healing from the perspective of spatial inflammation patterns. *Bioact. Mater.* **2023**, *28*, 243−254.

(5) Zhu, J.; Zhou, H.; Gerhard, E. M.; Zhang, S.; Parra Rodríguez, F. I.; Pan, T.; Yang, H.; Lin, Y.; Yang, J.; Cheng, H. Smart bioadhesives for wound healing and closure. *Bioact. Mater.* **2023**, *19*, 360−375.

(6) Xue, K.; Leng, T.; Wang, Y.; Li, S.; Li, Z.; Li, Z.; Mao, J.; Wang, X.; Zhang, X.; Lin, C.; et al. Metabolic-Efferocytosis Enabled Hydrogel Synergism Reprograms Immune Microenvironment for Promoting Diabetic Wound Repair. *Adv. Funct. Mater.* **2025**, No. 2420079.

(7) Huang, W.; Guo, Q.; Wu, H.; Zheng, Y.; Xiang, T.; Zhou, S. Engineered Exosomes Loaded in Intrinsic Immunomodulatory Hydrogels with Promoting Angiogenesis for Programmed Therapy of Diabetic Wounds. *ACS Nano* **2025**, *19* (14), 14467−14483.

(8) Meng, X.-m.; Wang, L.; Nikolic-Paterson, D. J.; Lan, H.-Y. Innate immune cells in acute and chronic kidney disease. *Nat. Rev. Nephrol.* **2025**, *21*, 464.

(9) Walsh, C. Molecular mechanisms that confer antibacterial drug resistance. *Nature* **2000**, *406* (6797), 775−781.

(10) Levy, S. B.; Marshall, B. Antibacterial resistance worldwide: causes, challenges and responses. *Nat. Med.* **2004**, *10* (12), S122−S129.

(11) Li, G.; Deng, H.; Xu, W.; Chen, W.; Lai, Z.; Zhu, Y.; Zhang, L.; Shao, C.; Shan, A. Combating Antibiotic-Resistant Bacterial Infection Using Coassembled Dimeric Antimicrobial Peptide-Based Nanofibers. *ACS Nano* **2025**, *19* (3), 3155−3171.

(12) Liu, H.; Song, Z.; Zhang, Y.; Wu, B.; Chen, D.; Zhou, Z.; Zhang, H.; Li, S.; Feng, X.; Huang, J.; Wang, H. De novo design of self-assembling peptides with antimicrobial activity guided by deep learning. *Nat. Mater.* **2025**, *24*, 1295.

(13) Li, C.; Cai, Z.; Wei, B.; Qu, L.; Yan, M.; Zhou, Z.; Liu, B.; Xu, J.; Sun, C.; Wang, Y.; et al. Synthesis of Cu-Ag Bimetallic Nanoparticle Hydrosols and Their Superior Antibacterial Performances for Control of Microbial Corrosion by Desulfovibrio Desulfuricans Biofilm. *Adv. Funct. Mater.* **2025**, *35*, No. 2500354.

(14) Li, Z.; Yang, T.; Li, X.; Yin, P.; Yang, B.; Li, D.; Wang, Y.; Teng, W.; Yu, Q.; Li, W. A Bio-Responsive Hydrogel with Spatially Heterogeneous Structure for Treating Infectious Tissue Injuries. *Adv. Sci.* **2025**, *12*, No. 2500088.

(15) Zhao, Y.; Zhao, S.; Du, Y.; Gao, Z.; Li, Y.; Ma, H.; Li, H.; Ren, X.; Fan, Q.; Wu, D.; Wei, Q. Inverse Oxide/Alloy-Structured Nanozymes with NIR-Triggered Enzymatic Cascade Regulation of ROS Homeostasis for Efficient Wound Healing. *Adv. Mater.* **2025**, *37* (14), No. 2418731.

(16) Zheng, Y.; Wang, S.; Jin, W.; Li, Z.; Yang, G.; Li, X.; Li, N.; Wang, Y.; Sheng, F.; Song, Z. An ultrasound-driven PLGA/Zn-KNN hybrid piezoelectric scaffold with direct and immunoregulatory antibacterial activity for bone infection. *Bioact. Mater.* **2025**, *47*, 295−312.

(17) Wang, Y.; Su, P.; Lin, Z.; Li, X.; Chen, K.; Ye, T.; Li, Y.; Zou, Y.; Wang, W. A Tribo/Piezoelectric Nanogenerator Based on Bio-MOFs for Energy Harvesting and Antibacterial Wearable Device. *Adv. Mater.* **2025**, *37* (9), No. 2418207.

(18) Vadlamani, A.; Detwiler, D. A.; Dhanabal, A.; Garner, A. L. Synergistic bacterial inactivation by combining antibiotics with nanosecond electric pulses. *Appl. Microbiol. Biotechnol.* **2018**, *102* (17), 7589−7596.

(19) Fernandes, M. M.; Carvalho, E. O.; Lanceros-Mendez, S. Electroactive Smart Materials: Novel Tools for Tailoring Bacteria Behavior and Fight Antimicrobial Resistance. *Front. Bioeng. Biotechnol.* **2019**, *7*, 277.

(20) Wang, G.; Feng, H.; Hu, L.; Jin, W.; Hao, Q.; Gao, A.; Peng, X.; Li, W.; Wong, K.-Y.; Wang, H.; et al. An antibacterial platform based on capacitive carbon-doped TiO2 nanotubes after direct or alternating current charging. *Nat. Commun.* **2018**, *9* (1), No. 2055.

(21) Mao, K.; Yue, M.; Ma, H.; Li, Z.; Liu, Y. Electro- and Magneto-Active Biomaterials for Diabetic Tissue Repair: Advantages and Applications. *Adv. Mater.* **2025**, *37*, No. 2501817.

(22) Lee, K. Y.; Mooney, D. J. Hydrogels for Tissue Engineering. *Chem. Rev.* **2001**, *101* (7), 1869−1880.

(23) Zhang, Y. S.; Khademhosseini, A. Advances in engineering hydrogels. *Science* **2017**, *356* (6337), No. eaaf3627.

(24) Molinaro, R.; Corbo, C.; Martinez, J. O.; Taraballi, F.; Evangelopoulos, M.; Minardi, S.; Yazdi, I. K.; Zhao, P.; De Rosa, E.; Sherman, M. B.; et al. Biomimetic proteolipid vesicles for targeting inflamed tissues. *Nat. Mater.* **2016**, *15* (9), 1037−1046.

(25) Keplinger, C.; Sun, J.-Y.; Foo, C. C.; Rothemund, P.; Whitesides, G. M.; Suo, Z. Stretchable, Transparent, Ionic Conductors. *Science* **2013**, *341* (6149), 984−987.

(26) Yuk, H.; Lu, B.; Zhao, X. Hydrogel bioelectronics. *Chem. Soc. Rev.* **2019**, *48* (6), 1642−1667.

(27) Mawad, D.; Mansfield, C.; Lauto, A.; Perbellini, F.; Nelson, G. W.; Tonkin, J.; Bello, S. O.; Carrad, D. J.; Micolich, A. P.; Mahat, M. M.; et al. A conducting polymer with enhanced electronic stability applied in cardiac models. *Sci. Adv.* **2016**, *2* (11), No. 1601007.
(28) Koetting, M. C.; Peters, J. T.; Steichen, S. D.; Peppas, N. A. Stimulus-responsive hydrogels: Theory, modern advances, and applications. *Mater. Sci. Eng. R* **2015**, *93*, 1−49.
(29) Polat, B. E.; Hart, D.; Langer, R.; Blankschtein, D. Ultrasound-mediated transdermal drug delivery: Mechanisms, scope, and emerging trends. *J. Controlled Release* **2011**, *152* (3), 330−348.
(30) Chen, Q.; Xu, L.; Liang, C.; Wang, C.; Peng, R.; Liu, Z. Photothermal therapy with immune-adjuvant nanoparticles together with checkpoint blockade for effective cancer immunotherapy. *Nat. Commun.* **2016**, *7* (1), No. 13193.
(31) Flowers, L.; Grice, E. A. The Skin Microbiota: Balancing Risk and Reward. *Cell Host Microbe* **2020**, *28* (2), 190−200.
(32) Constantinides, M. G.; Link, V. M.; Tamoutounour, S.; Wong, A. C.; Perez-Chaparro, P. J.; Han, S.-J.; Chen, Y. E.; Li, K.; Farhat, S.; Weckel, A.; et al. MAIT cells are imprinted by the microbiota in early life and promote tissue repair. *Science* **2019**, *366* (6464), No. eaax6624.
(33) Wynn, T. A.; Barron, L. Macrophages: Master Regulators of Inflammation and Fibrosis. *Semin. Liver. Dis.* **2010**, *30* (03), 245−257.
(34) Li, C.; Levin, M.; Kaplan, D. L. Bioelectric modulation of macrophage polarization. *Sci. Rep.* **2016**, *6* (1), No. 21044.
(35) da Silva, L. P.; Kundu, S. C.; Reis, R. L.; Correlo, V. M. Electric Phenomenon: A Disregarded Tool in Tissue Engineering and Regenerative Medicine. *Trends Biotechnol.* **2020**, *38* (1), 24−49.
(36) Yao, B.; Wang, H.; Zhou, Q.; Wu, M.; Zhang, M.; Li, C.; Shi, G. Ultrahigh-Conductivity Polymer Hydrogels with Arbitrary Structures. *Adv. Mater.* **2017**, *29* (28), No. 1700974.
(37) Zhou, C.; Wu, T.; Xie, X.; Song, G.; Ma, X.; Mu, Q.; Huang, Z.; Liu, X.; Sun, C.; Xu, W. Advances and challenges in conductive hydrogels: From properties to applications. *Eur. Polym. J.* **2022**, *177*, No. 111454.
(38) Mo, F.; Lin, Y.; Liu, Y.; Zhou, P.; Yang, J.; Ji, Z.; Wang, Y. Advances in ionic conductive hydrogels for skin sensor applications. *Mater. Sci. Eng. R* **2025**, *165*, No. 100989.
(39) Xia, Y.; Sun, K.; Ouyang, J. Solution-Processed Metallic Conducting Polymer Films as Transparent Electrode of Optoelectronic Devices. *Adv. Mater.* **2012**, *24* (18), 2436−2440.
(40) Kim, N.; Kee, S.; Lee, S. H.; Lee, B. H.; Kahng, Y. H.; Jo, Y.-R.; Kim, B.-J.; Lee, K. Highly Conductive PEDOT:PSS Nanofibrils Induced by Solution-Processed Crystallization. *Adv. Mater.* **2014**, *26* (14), 2268−2272.
(41) Yan, L.; Hao, J.; Liu, B.; Zou, X.; Wu, Q.; Hou, J.; Duan, J.; Wei, S.; Zhou, Y.; Xiang, B.; Hou, B. A universal design for triggering the precise micro-structure reconstruction through in-situ electro-regulating to boost the pseudocapacitance of MnO2. *J. Energy Chem.* **2022**, *74*, 184−197.
(42) Yedgar, S.; Barshtein, G.; Gural, A. Hemolytic Activity of Nanoparticles as a Marker of Their Hemocompatibility. *Micromachines* **2022**, *13* (12), 2091.
(43) Derakhshankhah, H.; Mohammad-Rezaei, R.; Massoumi, B.; Abbasian, M.; Rezaei, A.; Samadian, H.; Jaymand, M. Conducting polymer-based electrically conductive adhesive materials: design, fabrication, properties, and applications. *J. Mater. Sci. − Mater. Electron.* **2020**, *31* (14), 10947−10961.
(44) Lee, S.; Sasaki, D.; Kim, D.; Mori, M.; Yokota, T.; Lee, H.; Park, S.; Fukuda, K.; Sekino, M.; Matsuura, K.; et al. Ultrasoft electronics to monitor dynamically pulsing cardiomyocytes. *Nat. Nanotechnol.* **2019**, *14* (2), 156−160.
(45) Khaw, J. S.; Xue, R.; Cassidy, N. J.; Cartmell, S. H. Electrical stimulation of titanium to promote stem cell orientation, elongation and osteogenesis. *Acta Biomater.* **2022**, *139*, 204−217.
(46) Luo, R.; Dai, J.; Zhang, J.; Li, Z. Accelerated Skin Wound Healing by Electrical Stimulation. *Adv. Healthcare Mater.* **2021**, *10* (16), No. 2100557.
(47) Versey, Z.; da Cruz Nizer, W. S.; Russell, E.; Zigic, S.; DeZeeuw, K. G.; Marek, J. E.; Overhage, J.; Cassol, E. Biofilm-Innate Immune Interface: Contribution to Chronic Wound Formation. *Front. Immunol.* **2021**, *12*, No. 648554.
(48) Li, D.; Chen, K.; Tang, H.; Hu, S.; Xin, L.; Jing, X.; He, Q.; Wang, S.; Song, J.; Mei, L.; et al. A Logic-Based Diagnostic and Therapeutic Hydrogel with Multistimuli Responsiveness to Orchestrate Diabetic Bone Regeneration. *Adv. Mater.* **2022**, *34* (11), No. 2108430.
(49) Gray, D. A.; Wang, B.; Sidarta, M.; Cornejo, F. A.; Wijnheijmer, J.; Rani, R.; Gamba, P.; Turgay, K.; Wenzel, M.; Strahl, H.; Hamoen, L. W. Membrane depolarization kills dormant Bacillus subtilis cells by generating a lethal dose of ROS. *Nat. Commun.* **2024**, *15* (1), No. 6877.
(50) Lai, S.; Wang, Y.; Wan, Y.; Ma, H.; Fang, L.; Su, J. Magnetoelectric Polymer Membrane-Based Electrical Microenvironment with Magnetically Controlled Antibacterial Activity. *ACS Appl. Mater. Interfaces* **2022**, *14* (17), 20139−20150.
(51) Forbes, S. J.; Rosenthal, N. Preparing the ground for tissue regeneration: from mechanism to therapy. *Nat. Med.* **2014**, *20* (8), 857−869.
(52) Atamas, S. P. Complex cytokine regulation of tissue fibrosis. *Life Sci.* **2002**, *72* (6), 631−643.
(53) Zhou, Y.; Ma, X.; Yu, C.; Tian, Y.; Liang, Q.; Xin, M.; Sun, P.; Liu, F.; Chao, D.; Jia, X.; et al. A Wearable Self-Charging Electroceutical Device for Bacteria-Infected Wound Healing. *ACS Nano* **2024**, *18* (24), 15681−15694.
(54) Jiang, Y.; Trotsyuk, A. A.; Niu, S.; Henn, D.; Chen, K.; Shih, C.-C.; Larson, M. R.; Mermin-Bunnell, A. M.; Mittal, S.; Lai, J.-C.; et al. Wireless, closed-loop, smart bandage with integrated sensors and stimulators for advanced wound care and accelerated healing. *Nat. Biotechnol.* **2023**, *41* (5), 652−662.

https://doi.org/10.1021/acsami.5c13537
ACS Appl. Mater. Interfaces 2025, 17, 53232−53243

Supporting information

Chargeable hydrogels with dual modulatory effects of bacterial killing and immune remodeling towards wound healing

Yiheng Tang,[1#] Guopeng Xu,[1#] Jing Liu,[2#] Jiezhou Wu,[1] Jingyang Fang,[1] Shengji Gu,[1] Wenyan Zhang,[1] Wenkun Zhang,[1] Junfeng Hu,[1] Paul K. Chu,[3] Jianzhong Du,[4] Guomin Wang[1]*

[1] State Key Laboratory of Cardiovascular Diseases and Medical Innovation Center, Shanghai East Hospital, School of Medicine, Tongji University, Shanghai 200070, China.

[2] Tianjin Key Laboratory of Biomaterial Research, Institute of Biomedical Engineering, Chinese Academy of Medical Sciences and Peking Union Medical College, Tianjin, 300192, China.

[3] Department of Physics, Department of Materials Science and Engineering, and Department of Biomedical Engineering, City University of Hong Kong, Tat Chee Avenue, Kowloon 999077, Hong Kong.

[4] Department of Polymeric Materials, School of Materials Science and Engineering, Tongji University, 4800 Caoan Road, Shanghai 201804, China.

[*]Corresponding author. Email: wangguominhi@gmail.com

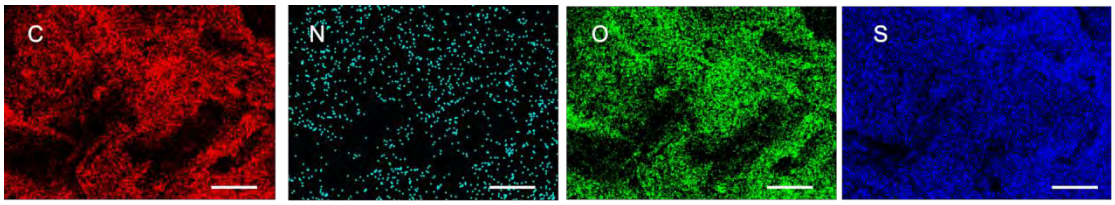

Figure S1. Elemental mappings of AT-PP by EDS. Scale bar: 100 μm.

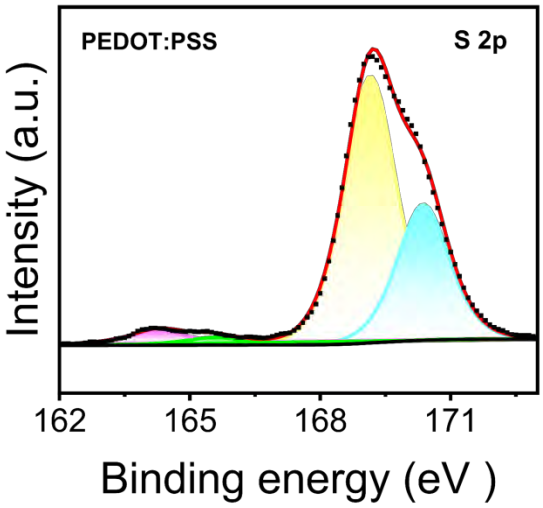

Figure S2. HR-XPS spectra of S 2p for freeze-dried PEDOT:PSS.

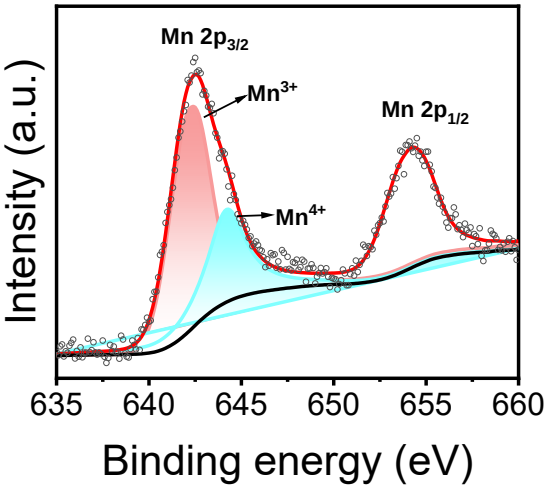

Figure S3. HR-XPS spectra of Mn 2p of freeze-dried AT-PP@MnO_2 before charging.

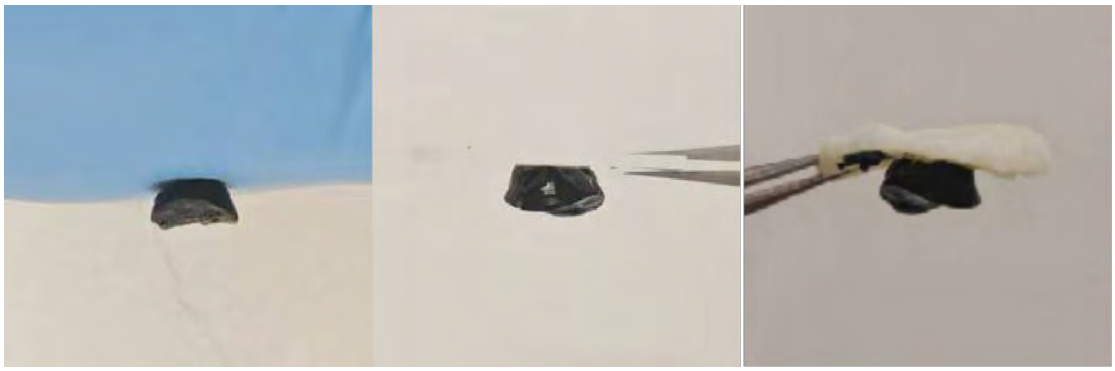

Figure S4. Adhesive performance evaluation of AT-PP@MnO_2 on nitrile gloves (left), glass (middle), and porcine skin (right).

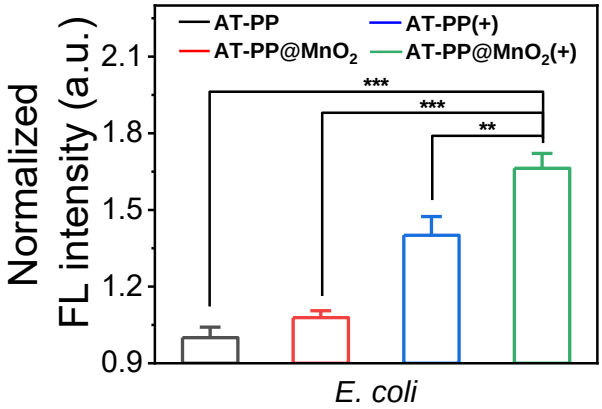

Figure S5. The variation of bacterial membrane potential for *E. coli* after various treatments. Data are presented as the mean ± S.D. with *, ** and *** denoting $p < 0.05$, $p < 0.01$ and $p < 0.001$, respectively.

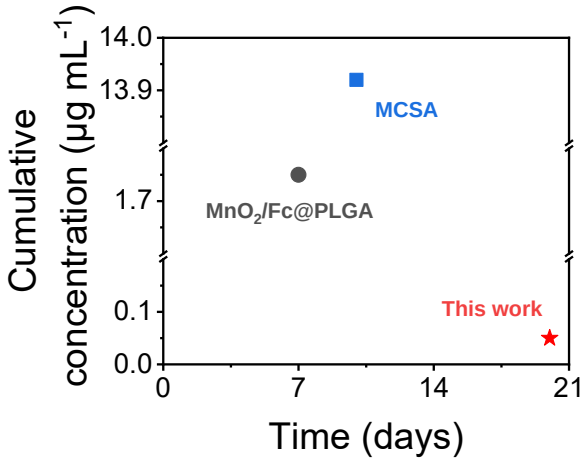

Figure S6. The cumulative Mn ion release of AT-PP@MnO2 in PBS solution (PH = 7.4) compared to other similar works.[1, 2]

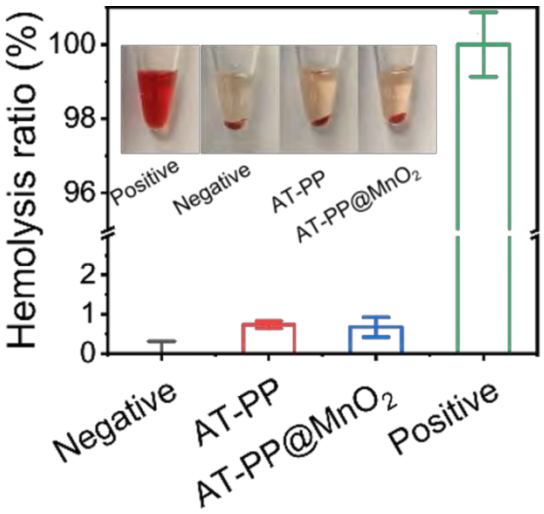

Figure S7. Hemolytic rate of red blood cells after incubation with different samples.

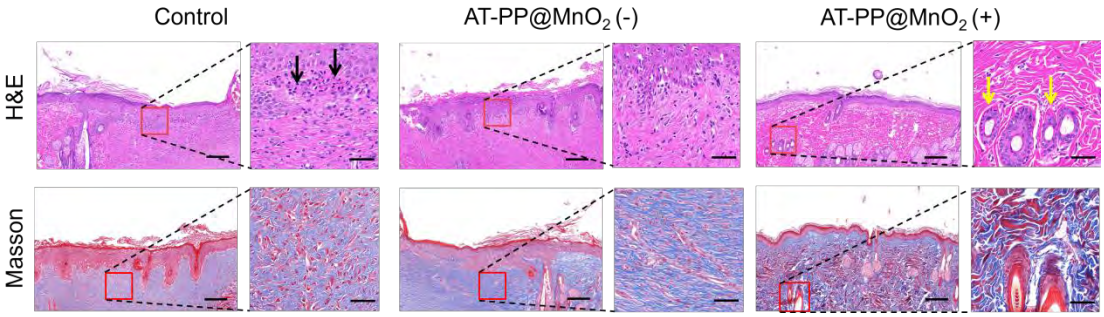

Figure S8. Representative (left) and magnified (right) images of H&E, and Masson staining of infected wounds after different treatments on day 14. Scale bar: 200 μm (left) and 50 μm (right).

(1) Wang, L.; Guo, H.; Zhang, W.; Li, X.; Su, Z.; Huang, X. Injectable hydrogels for Fenton-like Mn^{2+}/Fe^{2+} delivery with enhanced chemodynamic therapy prevent osteosarcoma recurrence and promote wound healing after excision surgery. *Mater. Today Bio* **2024**, *29*, 101297.
(2) Wu, Z.; Zhuang, H.; Ma, B.; Xiao, Y.; Koc, B.; Zhu, Y.; Wu, C. Manganese-Doped Calcium Silicate Nanowire Composite Hydrogels for Melanoma Treatment and Wound Healing. *Research* **2021**, *2021*, 101297.